

# PROCEEDINGS A

[rspa.royalsocietypublishing.org](http://rspa.royalsocietypublishing.org)

Research



Article submitted to journal

**Subject Areas:**

applied mathematics, materials science, math biology, differential equations

**Keywords:**

Oseen–Frank Theory, Liquid crystal, DNA, Helical configuration, Bifurcation, Filament reconstruction

**Author for correspondence:**

M. Carme Calderer

e-mail: [calde014@umn.edu](mailto:calde014@umn.edu)

## Helical organization of DNA-like liquid crystal filaments in cylindrical viral capsids

Pei Liu<sup>1</sup>, Javier Arsuaga<sup>2</sup>, M. Carme Calderer<sup>1</sup>, Dmitry Golovaty<sup>3</sup>, Mariel Vazquez<sup>4</sup>, Shawn Walker<sup>5</sup>

<sup>1</sup> School of Mathematics, University of Minnesota, Twin Cities, MN 55455, USA

<sup>2</sup> Department of Molecular and Cellular Biology, and Department of Mathematics, University of California, Davis, Davis, CA 95616, USA

<sup>3</sup> Department of Mathematics, University of Akron, Akron, OH 44325, USA

<sup>4</sup> Department of Mathematics, and Department of Microbiology and Molecular Genetics, University of California, Davis, Davis, CA 95616, USA

<sup>5</sup> Department of Mathematics, Louisiana State University, Baton Rouge, LA 70803, USA

We study equilibrium configurations of ds-DNA in a cylindrical viral capsid. We assume that the state of the encapsidated DNA consist of a disordered inner core enclosed by an ordered outer region, next to the capsid wall. In our approach, a DNA configuration is described by a unit helical vector field, tangent to an associated center curve, passing through properly selected locations. We postulate an expression for the energy of the encapsulated DNA based on that of columnar chromonic liquid crystals. A thorough analysis of the Euler–Lagrange equations yields multiple solutions to the corresponding boundary value problems. We demonstrate that there is a trivial, non-helical solution, together with two other solutions with nonzero helicity of the opposite sign. Using bifurcation analysis, we derive the conditions for local stability of such solutions and determine when the preferred coiling state is helical. The relevant bifurcation parameters are the ratio of the twist versus the bend moduli of DNA and the ratio between the sizes of the ordered and the disordered regions.

© The Authors. Published by the Royal Society under the terms of the Creative Commons Attribution License <http://creativecommons.org/licenses/by/4.0/>, which permits unrestricted use, provided the original author and source are credited.

## 1. Introduction

In this work, we study the packaging geometry of viral double-stranded (ds) DNA of tailed bacteriophages in idealized cylindrical capsids. The cylindrical geometry is taken as a coarse approximation of the actual capsid shapes, including icosahedral and prolate, found in ds-DNA bacteriophage viruses [1, 2, 3, 4, 5, 6, 7]. These viruses use a molecular motor to store their genome in the protein capsid, where the length of the genome is much larger than the characteristic size of the capsid. We apply data from experimentally characterized viruses, such as the average capsid size and the genome length, to infer properties of the condensed equilibrium states and their bifurcations by taking advantage of the explicit calculations allowed only in the cylindrical geometry. We postpone to future work the treatment of spherical and icosahedral capsids, where numerical approaches are required. We point out that our study does not address single-stranded, helical, RNA viruses, with cylindrical capsids, such as the tobacco mosaic virus [8].

Key stages of the bacteriophage cycle are the phage morphogenesis, which includes capsid assembly and dsDNA packaging, a high pressure quiescent or equilibrium state, and the delivery and infection of the bacterial host. The well-ordered organization of DNA within a viral capsid is essential to ensure efficient genome delivery.

There is an extensive and rich body of work on bacteriophage viruses, involving, both, imaging techniques and modeling. Leforestier [9] lists three main approaches, the *inverse axial spooling* model, the *ball of yarn* and the *liquid crystalline drop* models. The latter approach stemmed from the evidence gained from X-ray diffraction images of bacteriophages obtained during the 60's decade, and later confirmed by cryo-EM microscopy, which provided strong evidence of the *hexagonal* packaging of DNA in the capsid. This model exploits the hexagonal crystal structure locally determined by the points of intersection of the DNA segments on orthogonal planes. In this approach, hexagonally crystallized monodomains entirely fill the capsid volume, separated by defect walls and forming a structure analogous to the Twist Grain Boundary liquid crystal [10, 11]. Hexagonal phases have also been observed in-vitro, with highly concentrated DNA arranged in toroidal clusters [12, 13].

In the inverse axial spooling approach, the DNA winds from the capsid periphery to the centre following successive hoops [14, 15]. This model and the related DNA arrangement in toroids has been extensively used for several decades [15, 16]. Evidence that supports the so called *spool structural motif* has been provided by the cryo-EM observations of Olson et al. [2]. These show that the DNA genome of the phage T4 forms a highly condensed series of concentric layers, spaced about 2.36 nm apart, that tend to follow the contour of the inner wall of the protein capsid. Along these lines, the data obtained by Cerritelli et al. [1] suggests that the T7 genome is spooled around the capsid in approximately six coaxial shells in a quasi-crystalline packing. This evidence combined with previous studies of a series of isometric bacteriophages lead to conclude that the coiling organization of condensed DNA may apply to most dsDNA bacteriophages [17]. This underlying model has been applied in many different contexts such as measuring of forces [18] and packaging by molecular motor [19].

Other approaches include a ball of a string and spooling folded toroid [20, 21, 22, 23]. The corresponding vector field is tangential to the concentric circles centered on the axis of the cylinder [24, 25]. These approaches have been used in the case of spherical-like capsids; in particular, the ball of yarn packages the DNA as in the axial spooling case but following a spherical geometry. One important distinction among the different approaches is the modeling of the core. Information from imaging lacks precision in reference to the structure of the core. In the spooling approach, mostly associated with cylindrical shaped capsids, the core is simply left empty or filled with strands parallel to the capsid axis.

A common theme in implementing the previous approaches is in that they involve the optimization of an energy functional, very often using tools from Monte-Carlo or Brownian motion molecular dynamics. An inherent problem to such approaches is their computational cost, allowing to treat only small genomes. A novel modeling continuum approach is that by Klug and

Ortiz [26] based on the introduction of a unit director field, as in nematic liquid crystals, with a scalar variable representing the local density of DNA. An additional feature of the model is the inclusion of a phenomenological *cohesive* energy that penalizes changes of the (hexagonal) cross-section. The discretization of the energy, along with the application of the gradient flow method to optimize it, lead to the *torsionless toroidal solenoids*, as the preferred configuration, having lower energy than the inverse spooling structure.

In this paper, we consider the previously introduced continuum model that endows condensed DNA with a structure locally consisting of curvilinear segments (representing the DNA center axis) together with their orthogonal cross-sections [27]. Assigning these segments an effective diameter yields a plane hexagonal crystal structure on the intersecting planes. The capsid core is treated as an isotropic free boundary region representing the disordered state of the DNA. Accordingly, the energy consists of the nematic Oseen-Frank contribution penalizing changes of direction of the vector field (and, so that of the DNA axis), and the isotropic energy of the core. Moreover, for the class of helical vector fields 3.3, the former also accounts for the elastic energy associated with the disruption of the hexagonal cross-sectional structure (Remark 2.1 and [27]). Furthermore, since images reveal a sharp transition between the ordered and disordered regions of the capsid, we include a surface energy term that tends to minimize the surface area of the interface. One relevant aspect of our approach is that the core is determined by the competition between the bending energy of the ordered region and the isotropic penalty of the core. One relevant aspect of our model is that it allows for twist energy mostly neglected in earlier approaches. Intuitively, it has the effect of releasing bending energy and so affecting the size of the core. However, it does not account for torsion. Mathematically, a key signature of our approach is the vector field-filament structure as in models from nuclear and plasma physics ([28] and references therein). Although we minimize the energy to obtain the optimal vector field, subsequent integration provides the center line filament. This also solves the *connectivity* problem affecting the inverse spooling approaches. However, one drawback to our approach is in that the Oseen-Frank energy does not allow for singularities in the vector field (except for point defects in three-dimensions). This precludes accounting for the knots often observed in the DNA, issue that we will address in forthcoming work.

We also depart from earlier works where the DNA is organized in concentric circles, such as in the case of the inverse spooling. Instead, we follow the approach developed to study confinement of semiflexible polymers following helical vector field configurations [29]. In this approach, the unknown vector field  $\vec{n}$  is parameterized by the azimuthal angle  $\psi$ . In addition to providing connectivity, this approach allows us to incorporate twist deformations, as well as incorporating cholesteric effects. The rate of the bending versus twist modulus,  $\alpha := \frac{K_3}{K_2}$ , turns out crucial in determining how the DNA fills the capsid. Indeed, this parameter provides a quantitative justification for treating condensed DNA as a liquid crystal, and, in particular, endowing it with the Oseen-Frank energy. Values of  $\alpha$  used in our work stem from the DNA elasticity and viscosity studies found in [30].

By considering cylindrical capsids of radius  $R_2$  and height  $2h$ , we obtain exact expression for the critical values of  $\alpha$ . Through a bifurcation analysis, we identify the threshold value of  $\alpha$  below which concentric circles are the optimal organization structure, with helical states above. This result is reminiscent of that in [19] that simulates the filling of a capsid under the axial spooling structure, showing a transition between concentric circles organized as tori to such circles expanding along the capsid axis as the DNA fills the capsid. Our work also admits a natural extension to the case of spheroidal capsids and other general shapes. However, in such cases the optimization can only be done numerically, although similar patterns of behavior as for a cylindrical capsid are expected.

We also perform a stability analysis of the solutions and show that the states of four selected viruses fall within the stable helical branches, except for the virus T5, with slightly larger capsid diameter, which is classified within the stable concentric circle branch. The bifurcation structure between concentric circles and helical configurations extends a renowned result on nematic

liquid crystals placed between coaxial cylinders [31]. In the latter case, the bifurcation occurs between radial director field configurations and those parallel to the cylindrical axis. From a different point of view, the coexistence between the ordered and disorder DNA regions in the capsid follows the analogous *tactoid* texture phenomenon, observed in small molecule chromonic liquid crystals [32]. The paper concludes with the filament reconstruction. Choosing a point of entrance of the DNA into the capsid, we integrate the vector field along helical segments on the surface of a discrete family of concentric cylinders. The latter are separated by a distance equal to the pitch of the helix. There are two types of reconstruction according to whether the helices wind in the same or in opposite directions along alternating cylinders. In both cases, interpolation between strands is required at the top and bottom, with the parallel one taking the form of a *U-turn*, heuristically with higher bending energy than the first one. However, the inclusion of the electrostatic energy would be needed for conclusively sorting out between both such configurations. These constructions are presented in the Supplementary Materials. The helical inversion in liquid crystal materials has been found, specially in polymer dispersed liquid crystals, in connection with changes of temperature and radiation with ultraviolet light [33]. It is also naturally found in biological systems, although scarcely. For instance, a case remarkably similar to our alternating handedness construction has been reported in the protective tubular structures of the deep-sea worm, where the sign changes every 180° rotation [34]. A comprehensive overview on controlling and understanding the pitch inversion phenomenon is given in [35]. A recent review of viral growth and form can be found in [36]. Our work is also related to those on organization of confined polymers, also model as liquid crystals, both, in the achiral and chiral cases [37, 38]. Although in the current article we deal with two types of organization, that is, concentric circles and helices, a richer variety of structures has been observed in polymers. Specifically, spontaneous domain formation in spherically confined elastic filaments, shows that the ground state of the confined worm-like chain is an ordering mosaic of multiple homogeneously ordered domains, instead of a single spool [39].

The work is organized as follows. In section 2, we present the model to be analyzed. The main results are developed in section 3. In section 3 (a), we consider the case that the inner core radius  $R_1$  is fixed and neglect the energy of the core. Section 3 (b) is devoted to studying the Euler-Lagrange equations of the energy. The zero divergence condition reduces the problem to nonlinear ordinary differential equation for the angle of orientation of the director field. In section 3 (c), we perform the bifurcation analysis and the investigation of the stability of the different solution branches. Elliptic integrals play a main role in the analysis. In section 3 (d), we treat the core as a free boundary domain and incorporate the isotropic energy in the total form. The section ends with a discussion of the parameters of the model, showing that our results are along the line with actual data, for a set of four sample viruses. Section 4 is devoted to the filament reconstruction for alternating winding helices. In section 5, we present conclusions and discuss follow up work.

## 2. The Model

In our approach, the equilibrium states of the DNA packaged inside the capsid are associated with those of a unit vector field  $\vec{n}$ . The capsid is represented by a bounded, open domain  $\mathcal{B}$ , consisting of two subsets  $\Omega$  and  $\Omega_0$ , whose interiors are disjoint, and such that  $\mathcal{B} = \Omega \cup \Omega_0$ . The subset  $\Omega$  represents the region where the DNA is ordered whereas  $\Omega_0$  corresponds to the disordered one. In terms of the vector field approach, they represent the nematic and isotropic liquid crystal states, respectively. The unknown fields of the model are the vector field  $\vec{n}$  and the domain  $\Omega_0$ . We formulate the total energy accordingly, that is, as the sum of the constrained Oseen-Frank energy of the nematic plus the isotropic energy of the core region  $\Omega_0$ . That is,

$$E = \int_{\Omega} \left( K_3 |\vec{n} \times \nabla \times \vec{n}|^2 + K_2 (\tau + \vec{n} \cdot \nabla \times \vec{n})^2 \right) d\vec{x} + E_{disorder}(\Omega_0) \quad (2.1)$$

$$|\vec{n}| = 1 \text{ in } \Omega, \quad (2.2)$$

$$\nabla \cdot \vec{n} = 0 \text{ in } \Omega, \quad (2.3)$$

$$\vec{n} = \vec{n}_0 \text{ on } \partial\mathcal{B}, \quad (2.4)$$

$$\text{Vol}(\Omega) + \text{Vol}(\Omega_0) = \text{Vol}(\mathcal{B}). \quad (2.5)$$

The positive constants  $K_2$  and  $K_3$  denote the twist and bending moduli, respectively, and  $\tau$  is the chiral pitch. The zero constraint 2.3 on the splay is consistent with the columnar hexagonal nature of the ordered DNA, indicating that the number of filaments that enter an orthogonal unit area cross-section also exit it. That is, it guarantees that dislocations do not occur. We now recall a fundamental result in the analysis of the minimization of the Oseen-Frank energy of nematic liquid crystals, with density given by

$$\begin{aligned} \mathcal{W}_{OF} = & K_1(\nabla \cdot \vec{n})^2 + K_3|\vec{n} \times \nabla \times \vec{n}|^2 + K_2(\tau + \vec{n} \cdot \nabla \times \vec{n})^2 \\ & + (K_2 + K_4)(\text{tr}(\nabla \vec{n})^2 - (\nabla \cdot \vec{n})^2). \end{aligned} \quad (2.6)$$

The following inequalities on the Frank constants  $K_i$ , guaranteeing the coercivity of the total energy, play a main role in the analysis:

$$K_1 > 0, K_2 > 0, K_3 > 0, K_2 \geq |K_4|, 2K_1 \geq K_2 + K_4. \quad (2.7)$$

**Theorem 2.1.** [40] Let  $\mathcal{U} \in \mathbf{R}^3$  be an open and bounded set, with Lipschitz boundary  $\partial\mathcal{U}$ . Suppose that the Frank constants satisfy the inequalities (2.7). Let the admissible set be

$$\mathcal{A}(\vec{n}_0) = \{\vec{n} \in H^1(\mathcal{U}, \mathcal{S}^2) : \vec{n}|_{\partial\mathcal{U}} = \vec{n}_0\}$$

is nonempty. Then for any Lipschitz function  $\vec{n}_0 : \partial\mathcal{U} \rightarrow \mathcal{S}^2$ , the functional

$$E_{OF}(\vec{n}) := \int_{\mathcal{U}} \mathcal{W}_{OF}(\vec{n}, \nabla \vec{n}) d\vec{x} \quad (2.8)$$

admits a minimizer in  $\mathcal{A}(\vec{n}_0)$ . Furthermore, if  $\vec{n}$  is a minimizer of  $E_{OF}(\cdot)$ , then  $\vec{n}$  is analytic in  $\mathcal{U}/Z$  for some relatively closed subset  $Z$  of  $\mathcal{U}$  which has one dimensional Hausdorff measure zero.

Since the term multiplying  $(K_2 + K_4)$  in (2.6) is a null Lagrangian, and given that the boundary conditions imposed on the capsid wall are of Dirichlet type, without loss of generality, we set  $K_4 = 0$  and arrive at the expression (2).

**Remark 2.1.** The hexagonal columnar phase of chromonic liquid crystals can be characterized by an orthonormal set of vectors  $\{\vec{n}, \vec{m}, \vec{p}\}$ , the director  $\vec{n}$ , the liquid direction, describing the average alignment of the columnar axes, and the remaining pair of lattice vectors encoding the geometry of the crystal orthogonal cross-section. In order to account for the distortion of the lattice, an elastic energy term,  $\mathcal{W}_{Hex}(\vec{m}, \vec{p}, \nabla \vec{m}, \nabla \vec{p})$ , should be added to the integrand of the total energy 2.1. For the class of vector fields  $\vec{n}$  that we consider, including the cross-sectional energy amounts to replace the elastic constants  $K_2$  and  $K_3$  by effective values that account for the shear and bulk elastic modulus, but it does not otherwise affect the analysis presented here. This simplifying approach may have to be reconsidered if the goal is to predict the osmotic pressure in the capsid [27].

### 3. Main results

Henceforth, we will take the capsid to be a cylinder of radius  $R_2 > 0$  and height  $2h$ , which in cylindrical coordinates admits the representation  $\mathcal{B} = \{(r, z, \theta) | 0 \leq r \leq R_2, 0 \leq \theta < 2\pi, -h \leq z \leq h\}$ . For  $0 \leq R_1 \leq R_2$ , the region where the DNA is organized is expressed as

$$\Omega = \{(r, z, \theta) | R_1 \leq r \leq R_2, 0 \leq \theta < 2\pi, -h \leq z \leq h\}. \quad (3.1)$$

The disordered core is taken to be the inner cylinder  $\Omega_0 = \{(r, z, \theta) | 0 \leq r \leq R_1, 0 \leq \theta < 2\pi, -h \leq z \leq h\}$ , where  $R_1$ ,  $0 \leq R_1 \leq R_2$ , is either a prescribed number or an unknown of the problem. In the latter case, we associate to it an energy consistent with the isotropic liquid crystal phase.

Specifically, the assigned energy is equal to the sum of two contributions, one proportional to the inner core volume and, the second one proportional to the surface area separating the ordered and the disordered regions [27],

$$E_{disorder}[R_1] = 2h(\nu\pi R_1^2 + 2\sigma\pi R_1). \quad (3.2)$$

Here  $\nu > 0$  is the isotropic modulus and  $\sigma \geq 0$  is the surface tension.

We assume the director field  $\vec{n}$  (later identified with the unit tangent vector to the DNA center curve) takes the form,

$$\vec{n} = \cos \psi \cdot \vec{e}_\theta + \sin \psi \cdot \vec{e}_z, \quad (3.3)$$

where  $\psi(r, \theta, z) \in [-\pi/2, \pi/2]$  is a scalar function defined in  $\Omega$ .

### (a) Capsid with prescribed inner core: energy of the ordered region

We will first study the case when  $R_1 \geq 0$  is prescribed, neglecting the contribution  $E_{disorder}$ . The following theorem refers then to the total Oseen-Frank energy (2.8) of the liquid crystal in the domain  $\Omega$ , subject to the constraint (2.3).

**Theorem 3.1.** *Consider the total Oseen-Frank energy (2.8) in the cylindrical shell  $\Omega$ , with the prescribed inner and outer radii  $0 < R_1 < R_2$ . Let the Frank constants  $K_2, K_3 > 0$  also be given. Suppose that the constraint (2.3) holds and let  $\vec{n}$  be parameterized as in (3.3). Then the critical points of  $E_{OF}$  in  $H^1(\Omega)$  with natural boundary conditions, satisfy the following properties:*

- (i) *They are independent of  $\theta$  and  $z$ .*
- (ii) *There exists a smooth (local) energy minimizing configuration  $\psi(r)$ ,  $r \in (R_1, R_2)$ . Moreover, for achiral energies,  $\tau = 0, -\psi(r)$  is also a minimizer with the same energy. The scalar fields,  $\pm\psi$  determine helical vector fields of opposite handedness.*
- (iii) *In the case of a chiral material,  $\tau \neq 0$ , if  $\psi(r)$  is a minimizer, then  $-\psi(r)$  is also a minimizer of  $E_{OF}$  with the chiral pitch  $-\tau$ .*

*Proof.* For  $\vec{n}$  of the form (3.3), the Oseen-Frank energy reduces to,

$$\begin{aligned} E_{OF} = & \int_{\Omega} \left[ K_3 \left( \left( \frac{\cos^2 \psi}{r} \right)^2 + \left( \frac{\cos^2 \psi}{r} \psi_\theta + \frac{\sin(2\psi)}{2} \psi_z \right)^2 + \left( \frac{\sin(2\psi)}{2r} \psi_\theta + \sin^2 \psi \psi_z \right)^2 \right) \right. \\ & \left. + K_2 \left( \frac{\sin(2\psi)}{2r} - \psi_r + \tau \right)^2 \right] d\vec{x} \end{aligned} \quad (3.4)$$

The constraint  $\nabla \cdot \vec{n} = 0$  becomes

$$\psi_z = \frac{\tan \psi}{r} \psi_\theta. \quad (3.5)$$

Substituting the latter into the Oseen-Frank energy, it further simplifies to,

$$E_{OF}[\psi(r, \theta, z)] = \int_{\Omega} \left[ K_3 \left( \left( \frac{\cos^2 \psi}{r} \right)^2 + \frac{1}{r^2 \cos^2 \psi} \psi_\theta^2 \right) + K_2 \left( \frac{\sin(2\psi)}{2r} - \psi_r + \tau \right)^2 \right] d\vec{x} \quad (3.6)$$

$$\geq \int_{\Omega} \left[ K_3 \left( \frac{\cos^2 \psi}{r} \right)^2 + K_2 \left( \frac{\sin(2\psi)}{2r} - \psi_r + \tau \right)^2 \right] d\vec{x} \quad (3.7)$$

$$= \int_{-h}^h \int_0^{2\pi} \int_{R_1}^{R_2} \left[ K_3 \left( \frac{\cos^2 \psi}{r} \right)^2 + K_2 \left( \frac{\sin(2\psi)}{2r} - \psi_r + \tau \right)^2 \right] r dr d\theta dz \quad (3.8)$$

$$\triangleq E_{order}[\psi(r, \theta, z)]. \quad (3.9)$$

We point out that a critical point of  $E_{order}[\psi(r, \theta, z)]$ , which satisfies  $\frac{\delta E_{order}}{\delta \psi} = 0$ , where the symbol  $\delta$  refers to the total variation of  $E_{OF}$  with respect to  $\psi(r)$ , satisfies

$$-K_2 [(r\psi_r)]_r + \frac{\sin(2\psi)}{2r} (K_2 \cos(2\psi) - 2K_3 \cos^2 \psi) = \tau(\cos(2\psi) + 1). \quad (3.10)$$

The boundary conditions also result from setting the first variation of the energy equals to zero, that is

$$2r\psi_r \pm \sin(2\psi) = 0 \quad \text{or} \quad \psi = C, \quad (3.11)$$

at  $r = R_1$  and  $r = R_2$ , where  $C$  is a suitably chosen constant. Here the '+' sign corresponds to  $r = R_1$  and the '-' sign to  $r = R_2$ . The difference of signs is due to the opposite directions of the outer normal at two different boundary components.

In general, the solution to (3.10) and (3.11) may depend on  $(\theta, z)$  as parameters. However, the solution, which corresponds to the energy minimizer, is independent of  $\theta$  and  $z$ , thus

$$E_{\text{order}}[\psi(r, \theta, z)] \geq E_{\text{order}}[\psi(r)]. \quad (3.12)$$

We observe the critical points of the energy, that is solutions of the Euler-Lagrange equation (3.10) are smooth for  $r > 0$ . It follows from standard theory of ordinary differential equations [41].  $\square$

**Remark 3.1.** *Theorem 3.1 relies on the cylindrical geometry. If we consider the spherical domain, then the Oseen–Frank energy is minimized with  $\psi$  dependent on all three coordinates  $r, \theta$  and  $z$ .*

In view of Theorem 3.1, from now on, we will only consider axisymmetric solutions  $\psi(r)$ . We also note that there exists a constant trivial solution to Eq. (3.10), which is  $\psi = \frac{\pi}{2}$ . It describes the configuration of the director field to be parallel straight lines pointing from the bottom to the top, corresponding to the spiral-fold model [42] which is not discussed in this paper. If we further assume the chirality  $\tau = 0$ , then  $\psi = 0$  is also a constant trivial solution, which describes the director field tangent to concentric circles.

In what follows, we first discuss the case  $\tau = 0$ ; we will return to configurations with non-zero chirality in later sections. For physical consistency, we impose the natural boundary condition at  $R_1$ :  $2R_1\psi_r(R_1) + \sin(2\psi(R_1)) = 0$ , and the Dirichlet condition at  $R_2$ :  $\psi(R_2) = 0$ . This setup describes a liquid crystal, with the director field circularly anchored to the outer surface and free on the inner one. The concentric-circle configuration can be viewed as a 2-dimensional liquid crystal structure, while the 3-dimensional helical configuration corresponds to non-constant  $\psi(r) \neq 0$ . The transition from the concentric-circle to helical solutions, is a type of "escape to the third dimension" in nematic liquid crystals confined to cylinders [43].

We first study the existence of the helical solution and the stability of, both, the concentric-circle and helical solutions, under different set of parameters.

## (b) Solution of the Euler-Lagrange equations

We consider the governing equation (3.10), with  $\tau = 0$ , subject to the boundary conditions

$$\begin{cases} 2r\psi_r + \sin(2\psi) = 0, & \text{at } r = R_1; \\ \psi = 0, & \text{at } r = R_2. \end{cases} \quad (3.13)$$

We observe that the trivial solution  $\psi(r) = 0$  satisfies both boundary conditions, with the corresponding vector field  $\vec{n}$  being tangent to concentric circles.

Next, we focus on nontrivial solutions  $\psi \neq 0$ , with  $\vec{n}$  tangent to families of helical curves. For this we introduce the parameter

$$\alpha = \frac{K_3}{K_2}, \quad (3.14)$$

that will turn out to be pivotal in classifying the solutions of the equation. We first note that, integrating both sides of equation (3.10), after pre-multiplying by  $\psi_r$ , yields the first integral

$$(r\psi_r)^2 - \frac{\alpha}{2} \cos(2\psi) - \frac{1-\alpha}{8} \cos(4\psi) = C, \quad (3.15)$$

with  $C$  being an arbitrary constant. Using the boundary condition at  $r = R_1$ , the constant  $C$  can be expressed as

$$C = \frac{1}{4} \sin^2(2\psi(R_1)) - \frac{\alpha}{2} \cos(2\psi(R_1)) - \frac{1-\alpha}{8} \cos(4\psi(R_1)). \quad (3.16)$$

Equation (3.15) can be integrated once more. The solution satisfying the boundary condition  $\psi(R_2) = 0$ , is given by the elliptic integral

$$\frac{F\left(\arcsin\left(\sqrt{\frac{m_2}{1-m_2}} \tan \psi\right) \middle| \frac{m_1(1-m_2)}{m_2(1-m_1)}\right)}{\sqrt{(1-\alpha)(1-m_1)m_2}} = \pm \ln \frac{R_2}{r}. \quad (3.17)$$

Here  $F(x|m) = \int_0^x \frac{d\theta}{\sqrt{1-m \sin^2 \theta}}$  is the elliptic integral of the first kind, with

$$m_{1,2} = \frac{(1-2\alpha)/2 \pm \sqrt{\alpha^2/4 + (1-\alpha)^2/8 - (1-\alpha)C}}{1-\alpha}.$$

Detailed derivation of (3.17) is given in the supplementary material section.

To determine the constant  $C$  or, equivalently,  $\psi(R_1)$ , we need to consider the boundary condition (3.13) at  $R_1$  and solve the resulting equation

$$\frac{F\left(\arcsin\left(\sqrt{\frac{m_2}{1-m_2}} \tan \psi(R_1)\right) \middle| \frac{m_1(1-m_2)}{m_2(1-m_1)}\right)}{\sqrt{(1-\alpha)(1-m_1)m_2}} = \pm \ln \frac{R_2}{R_1} \triangleq \pm M. \quad (3.18)$$

We note that  $\psi(R_1)$  depends on  $R_2$  through the ratio  $R_2/R_1$  only, and  $M \triangleq \ln \frac{R_2}{R_1}$  turns out to be an important parameter in later sections.

We observe that, when  $R_1 \rightarrow 0$  with fixed  $R_2$ , or when  $\alpha \rightarrow 1$ , equation (3.18) may not be properly defined. The first case corresponds to the DNA being fully ordered in the whole capsid, whereas the second one corresponds to the limit of equal twist and bending effects. Next, let us carefully analyze these two special cases, and then the general situation.

### (i) $R_1 = 0$

The energy of the system reduces to

$$E_{order} = 4\pi h K_2 \int_0^{R_2} \left[ \left| \frac{\sin(2\psi)}{2r} - \psi_r \right|^2 + \alpha \frac{\cos^4 \psi}{r^2} \right] r dr. \quad (3.19)$$

The boundary condition  $2r\psi_r + \sin(2\psi) = 0$  at  $r = 0$  indicates  $\psi(0) = 0$  or  $\pi/2$ .

If  $\psi(0) = 0$ , the first integral becomes,

$$(r\psi_r)^2 = -\alpha \sin^2(\psi) - \frac{1-\alpha}{4} \sin^2(2\psi). \quad (3.20)$$

We point out that, for given  $K_2, K_3 > 0$ , the right hand side of the previous equation is non-positive. Thus, only the trivial solution  $\psi(r) = 0$  exists.

Next, we focus on the case that  $\psi(0) = \pi/2$ . The first integral (3.15) and (3.16) becomes

$$(r\psi_r)^2 = \alpha \cos^2(\psi) - \frac{1-\alpha}{4} \sin^2(2\psi). \quad (3.21)$$

Integrating it once more, we get

$$\frac{1}{\sqrt{2\alpha-1}} \tanh^{-1} \left( \frac{\sqrt{2\alpha-1} \sin(\psi)}{\sqrt{2\alpha-1 + (1-\alpha) \cos^2 \psi}} \right) = \pm \ln \frac{r}{R_2}, \quad (3.22)$$

which implicitly defines the function  $\psi(r)$ . In the special case  $\alpha = 1$ , it becomes

$$\psi = \pm \arcsin \frac{R_2^2 - r^2}{R_2^2 + r^2} = \pm \arccos \frac{2rR_2}{R_2^2 + r^2}. \quad (3.23)$$

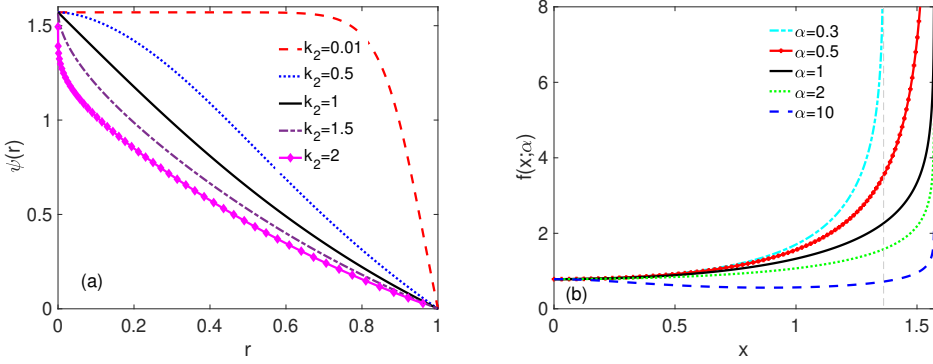


**Figure 1.** (a) Solution  $\psi(r)$  given by Eq. (3.22), with  $R_1 = 0$ ,  $R_2 = 1$ ,  $K_3 = 1$  and different  $K_2$ . (b) The graph of function  $f(x; \alpha)$  for different values of  $\alpha$ . The curves with  $\alpha = 0.5, 1, 2, 10$  have a vertical asymptote at  $x = \pi/2$ . The vertical asymptote for  $\alpha = 0.3$  is  $x = \beta(\alpha) < \pi/2$ . The curves with  $\alpha = 0.3, 0.5, 1, 2$  are monotone increasing, while the curve for  $\alpha = 10$  is decreasing then increasing.

Likewise, for  $\alpha = 1/2$ , the explicit form of the solution is

$$\psi = \pm \arctan(\ln(R_2/r)/\sqrt{2}). \quad (3.24)$$

The graphs of  $\psi(r)$ , for different values of  $\alpha$ , are shown in Fig. 1 (a).

**Remark 3.2.** For  $\alpha < 1/2$ , Eq. (3.22) does not have real solutions, indicating that the boundary conditions in (3.13) fail. Hence only the solutions with  $\vec{n}$  tangent to concentric circles exist.

**Remark 3.3.** For  $\alpha \geq 1/2$ , the configurations given by (3.22) have finite energy,  $E_{\text{order}}$ , and it is independent of  $R_2$ . (See Supplementary Material for the proof.)

### (ii) $\alpha = 1$ with $R_1 > 0$

In this special case, the first integral becomes,

$$(r\psi_r)^2 - \frac{1}{2} \cos(2\psi) = C, \quad (3.25)$$

Using the boundary condition at  $r = R_1$ , then  $C = \frac{\sin^2(2\psi(R_1))}{4} - \frac{1}{2} \cos(2\psi(R_1))$ , and

$$r\psi_r = \pm \sqrt{C + \cos(2\psi)/2}. \quad (3.26)$$

Integrating (3.25) again and applying the boundary condition  $\psi(R_2) = 0$ , we have

$$\frac{1}{\sqrt{m}} F(\psi | \frac{1}{m}) = \pm \ln \frac{r}{R_2}. \quad (3.27)$$

Here  $m = C + \frac{1}{2} = \frac{\sin^2(2\psi(R_1))}{4} + \sin^2(\psi(R_1))$ , and  $F(x|m) = \int_0^x \frac{d\theta}{\sqrt{1 - m \sin^2 \theta}}$  is the elliptic integral of the first kind.

In order to determine  $\psi(R_1)$ , we need to solve the following equation:

$$\frac{1}{\sqrt{m}} F(\psi(R_1) | \frac{1}{m}) = \pm M. \quad (3.28)$$

Let us define

$$f(x) \triangleq \frac{2F(x|\frac{4}{\sin^2(2x)+4\sin^2(x)})}{\sqrt{\sin^2(2x)+4\sin^2(x)}} = \frac{2x}{\sqrt{\sin^2(2x)+4\sin^2(x)}} \int_0^1 \frac{du}{\sqrt{1-\frac{4\sin^2(xu)}{\sin^2(2x)+4\sin^2(x)}}}. \quad (3.29)$$

This allows us to rewrite Eq. (3.28) as  $f(\psi(R_1)) = \pm M$ , with  $M$  as in (3.18). The results of this subsection are summarized in the following theorem and the proof is in the Supplementary Material.

**Theorem 3.2.** *Let  $\alpha = 1$  in equation (3.14). Then there exists a unique positive solution  $\psi(R_1) := c > 0$  to Eq. (3.28) if and only if  $\frac{R_2}{R_1} > e^{\pi/4} \approx 2.19328$ . Likewise,  $\psi(R_1) = -c < 0$  is the only negative solution. Furthermore, the functions  $\psi(r)$  given by Eq. (3.27), with  $\psi(R_1) = \pm c$ , are the only two non-trivial solutions of Eq. (3.10) satisfying the boundary conditions (3.13).*

**Remark 3.4.** *For  $\frac{R_2}{R_1} = e^{\frac{\pi}{4}}$ , we define  $f(0) = \lim_{x \rightarrow 0} f(x) = \frac{\pi}{4}$ . Then Eq. (3.27) has a solution satisfying  $\psi(R_1) = 0$ , which corresponds to the trivial solution  $\psi(r) \equiv 0$ .*

**Remark 3.5.** *When  $R_1 \rightarrow 0$ , so that  $\frac{R_2}{R_1} \rightarrow \infty$ , the solution  $\psi(r)$  satisfies  $\psi(R_1) \rightarrow \frac{\pi}{2}$ . This is consistent with the result from Section (i).*

### (iii) General Cases

Now we revisit Eq. (3.10), and analyze the general case  $\alpha \geq 0$  and  $R_1 > 0$  prescribed. Instead of formally using the elliptic integral, we start again from the first integral, and consider the function,

$$\begin{aligned} f(x; \alpha) &= \int_0^x \frac{dt}{\sqrt{\frac{\alpha}{2}(\cos(2t) - \cos(2x)) + \frac{1-\alpha}{8}(\cos(4t) - \cos(4x)) + \frac{1}{4}\sin^2(2x)}} \\ &= \int_0^1 \frac{x du}{\sqrt{(1-\alpha)\sin^4(xu) - \sin^2(xu) + 2\sin^2(x) - (2-\alpha)\sin^4(x)}}. \end{aligned} \quad (3.30)$$

Notice that,  $f(x; \alpha = 1)$  is the same function of  $x$  as  $f(x)$  in Eq. (3.29). By definition, and in analogy with Eq. (3.28), Eq. (3.18) can be rewritten as,

$$f(\psi(R_1); \alpha) = \pm M = \pm \ln \frac{R_2}{R_1}. \quad (3.31)$$

The properties of  $f$  should give us sufficient information on the solution  $\psi(r)$ . Furthermore, since  $f(x; \alpha)$  is an odd function of  $x$ , we only need to consider the positive sign in Eq. (3.31). Let us define,

$$G(u, x; \alpha) = (1-\alpha)\sin^4(xu) - \sin^2(xu) + 2\sin^2(x) - (2-\alpha)\sin^4(x), \quad (3.32)$$

for  $x \in [0, \pi/2]$  and  $u \in [0, 1]$ . Note that  $G$  is continuously differentiable with respect to, both,  $x$  and  $u$ . With  $x$  fixed,  $G(u, x; \alpha)$  can be viewed as a function of  $u$  only. We now discuss the properties of  $G$  and  $f$ , for two distinct ranges of values of  $\alpha$ , that is,  $\alpha \geq \frac{1}{2}$  and  $\alpha < \frac{1}{2}$ . The conclusions are based on calculating the derivative of  $G$  with respect to  $u$ .

When  $\alpha \geq 1/2$ , there is no interior critical point with respect to  $u$ , thus the extreme values of  $G$  can only occur at the end points  $u = 0$  or  $u = 1$ . Moreover, it is easy to check that  $G(0, x; \alpha) > 0$  and  $G(1, x; \alpha) > 0$ , for all  $x \in (0, \pi/2)$ , and so  $G(u, x; \alpha) > 0$  for all  $x \in (0, \pi/2)$  and  $u \in [0, 1]$ . Hence

$f(x; \alpha)$  is defined properly as a real function in  $0 < x < \pi/2$ . We can further calculate the limit,

$$\lim_{x \rightarrow \pi/2} f(x; \alpha) = \infty, \quad \text{if } \alpha \geq 1/2. \quad (3.33)$$

When  $\alpha < 1/2$ , there is no interior critical point of  $G$  with respect to  $u$ , for  $x \in (0, x_0]$ , with  $x_0 = \arcsin(\sqrt{\frac{1}{2-2\alpha}})$ . Thus the arguments used for the case  $\alpha \geq \frac{1}{2}$  still hold; hence  $f(x; \alpha)$  is a real function in  $(0, x_0]$ . For  $x \in (x_0, \pi/2)$ , there is one interior critical point of  $G(u, x; \alpha)$ , that is  $u_0 = \frac{x_0}{x}$ . Since  $G(u_0(x), x; \alpha)$  is monotonically decreasing in  $x \in [x_0, \pi/2]$ ,  $G(1, x_0; \alpha) > 0$  and  $G(2x_0/\pi, \pi/2; \alpha) < 0$ , there must exist one  $\beta \in (x_0, \pi/2)$ , such that  $G(u_0(x), x; \alpha) < 0$  for all  $x \in (\beta, \pi/2)$  and  $G(u_0(x), x; \alpha) > 0$  for all  $x \in (x_0, \beta)$ . When  $x \in (\beta, \pi/2)$ ,  $f(x; \alpha)$  becomes complex because  $\sqrt{G(u, x; \alpha)}$  is pure imaginary near  $u = u_0(x)$ . When  $x \in (0, \beta)$ ,  $f(x; \alpha)$  is real. For  $x = \beta$ , since  $G(x_0/\beta, \beta; \alpha) = G_u(x_0/\beta, \beta; \alpha) = 0$ , the integral  $\int G^{-1/2} du$  diverges, thus

$$\lim_{x \rightarrow \beta} f(x; \alpha) = \infty, \quad \text{if } \alpha < 1/2. \quad (3.34)$$

In both cases,  $\alpha \geq 1/2$  and  $\alpha < 1/2$ , we get the common limit

$$\lim_{x \rightarrow 0} f(x; \alpha) = \int_0^1 \frac{du}{\sqrt{2-u^2}} = \frac{\pi}{4}. \quad (3.35)$$

Proceeding with the Taylor expansion of  $f(x; \alpha)$  about  $x = 0$ , we get higher order corrections to the previous limit, that is,

$$\begin{aligned} f(x; \alpha) &\sim \int_0^1 \left( 1 - \frac{(1-\alpha)u^4 + u^4/3 - 2/3 + (\alpha-2)x^2}{4-2u^2} x^2 \right) \frac{du}{\sqrt{2-u^2}} \\ &= \frac{\pi}{4} - x^2 \left( \frac{2-\pi}{2} + \frac{3\pi-8}{8} \alpha \right). \end{aligned} \quad (3.36)$$

Hence, it follows that  $f'(0; \alpha) = 0$ , and  $f''(0; \alpha) > 0$ , when  $\alpha < \frac{4\pi-8}{3\pi-8}$ ;  $f''(0; \alpha) < 0$ , when  $\alpha > \frac{4\pi-8}{3\pi-8}$ . The graphs of  $f(x; \alpha)$ , for different values of  $\alpha$ , are shown in Fig. 1 (b).

**Remark 3.6.** Numerical calculation shows  $f(x; \alpha)$  is monotone increasing when  $\alpha \leq \frac{4\pi-8}{3\pi-8}$ , and  $f(x; \alpha)$  has one local minimum when  $\alpha > \frac{4\pi-8}{3\pi-8}$ .

We point out that, for  $\alpha$  small,  $f(x; \alpha)$  is monotone increasing. For  $\alpha$  large,  $f(x; \alpha)$  has an interval of decrease followed by one of increase, as  $x$  grows. Here, we omit the detailed calculation of the study of the monotonicity of  $f(x; \alpha)$ . Since it is very tedious, and instead, we refer to the numerical calculations shown in Fig. 1. We summarize the previous results as follows:

- (i) When  $0 \leq \alpha < 1/2$ , then  $f(x; \alpha)$  is a real, monotone increasing function in  $(0, \beta(\alpha)) \in (0, \pi/2)$ , whose range is  $(\pi/4, \infty)$ . A non-trivial solution to Eq. (3.31) exists if  $M > \pi/4$ , and the solution is unique.
- (ii) When  $\alpha \geq 1/2$ , then  $f(x; \alpha)$  is real in  $(0, \pi/2)$ . If  $f(x; \alpha)$  is monotone increasing, then its range is  $(\pi/4, \infty)$ , and a non-trivial solution to Eq. (3.31) exists if  $\ln(R_2/R_1) > \pi/4$ ; the solution is unique. If  $f(x; \alpha)$  is not monotone, then its range is  $[a, \infty)$  with some  $a < \pi/4$ . A non-trivial solution to Eq. (3.31) exists if  $M = \ln(R_2/R_1) > a$ , and the solution is not unique if  $a < M < \pi/4$ . We point out that  $a$  is the minimum of  $f(x; \alpha)$ .
- (iii) In all cases, the nontrivial solution  $\psi(r)$  depends on  $R_2$  only through the ratio  $\frac{R_2}{R_1}$ . Likewise, the dependence on the elasticity constants is solely through the ratio  $\alpha = \frac{K_3}{K_2}$ .

### (c) Stability of solutions

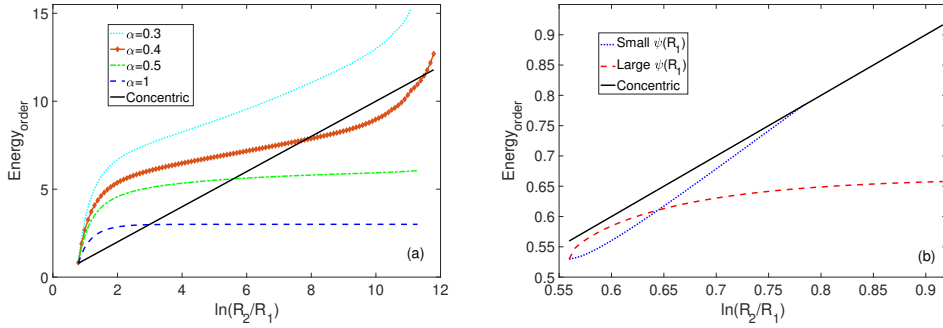


**Figure 2.** Total energy of the system for different configurations and parameter values. In both graphs, the black line is the plot of the energy of the concentric circle configuration. The coefficient  $4\pi h K_3$  is omitted for all the curves. Panel (a) shows the plot of the helical configurations for  $\alpha = 0.3, 0.4, 0.5$  and  $1$ . Panel (b) corresponds to  $\alpha = 10$ . There are two helical solutions with different positive  $\psi(R_1)$ . The figure shows the energy of both helical configurations.

### (i) Local stability of the helical solution $\psi(r)$

We consider a small perturbation  $\delta\psi(r) \in H_0^1([R_1, R_2])$  about the helical solution  $\psi(r)$ . It changes the energy by the amount

$$\begin{aligned} \delta E_{order} &= 4\pi h K_2 \int_{R_1}^{R_2} \left[ [\cos(2\psi)\delta\psi - r\delta\psi_r]^2 - [\sin(2\psi) - 2r\psi_r] \sin(2\psi)(\delta\psi)^2 \right. \\ &\quad \left. + 6\alpha \cos^2 \psi \sin^2 \psi (\delta\psi)^2 - 2\alpha \cos^4 \psi (\delta\psi)^2 \right] \frac{dr}{r}. \end{aligned}$$

Let  $x = \ln r - \ln R_1$  and recall that  $M = \ln R_2 - \ln R_1$ . Then

$$\delta E_{order} = 4\pi h K_2 \int_0^M \left[ (\delta\psi_x)^2 + [\cos(4\psi) + \frac{3\alpha}{2} \sin^2(2\psi) - 2\alpha \cos^4 \psi](\delta\psi)^2 \right] dx, \quad (3.37)$$

$$\geq 4\pi K_2 h \int_0^M \left[ \cos(4\psi) + \frac{3\alpha}{2} \sin^2(2\psi) - 2\alpha \cos^4 \psi + \frac{\pi^2}{M^2} \right] (\delta\psi)^2 dx. \quad (3.38)$$

Here we applied Wirtinger's inequality. The equality holds when  $\delta\psi \propto \sin(\pi x/M)$ . This allows us to establish the following theorem, and the proof is in the Supplementary Material.

**Theorem 3.3.** *The helical solution  $\psi(r)$  is stable in the following cases:*

- (i) If  $0 \leq \alpha \leq \frac{4}{5}$ , when  $M = \ln(R_2/R_1) \leq \pi/\sqrt{1 - \alpha + \frac{\alpha^2}{8(1-\alpha)}}$ ;
- (ii) If  $\alpha > \frac{4}{5}$ , when  $M = \ln(R_2/R_1) \leq \pi/\sqrt{2\alpha - 1}$ .

**Remark 3.7.** *Theorem 3.3 provides sufficient, but not necessary conditions for stability.*

### (ii) Local stability of concentric circles solution $\psi = 0$

Let us consider a small perturbation  $\delta\psi(r) \in H_0^1([R_1, R_2])$  about the solution  $\psi(r) = 0$ . The corresponding change in the energy is

$$\delta E_{order} = 4\pi h K_2 \int_0^M \left[ (1 - 2\alpha)(\delta\psi)^2 + (\delta\psi_x)^2 \right] dx \geq 4\pi h K_2 \int_0^M \left[ 1 - 2\alpha + \frac{\pi^2}{M^2} \right] (\delta\psi)^2 dx. \quad (3.39)$$

We now establish the following theorem, and the proof is in the Supplementary Material.

**Theorem 3.4.** *The concentric circle solution  $\psi(r) = 0$  has the following properties:*

- (i) *It is stable, provided  $0 \leq \alpha \leq 1/2$ , or  $\alpha > 1/2$  and  $M = \ln(R_2/R_1) < \pi/\sqrt{2\alpha - 1}$ .*
- (ii) *It is unstable, if  $\alpha > 1/2$  and  $M = \ln(R_2/R_1) > \pi/\sqrt{2\alpha - 1}$ .*

**Remark 3.8.** *When the concentric circle solution is unstable, we expect the helical solution to be stable, although it might not satisfy the conditions of Theorem 3.4.*

### (iii) Energy comparison

We now compare the energy of the concentric circle solution with that of the helical one. The former can be explicitly calculated as

$$E_{\text{order}}[\psi(r) = 0] = 4\pi h K_2 \alpha \int_{R_1}^{R_2} \frac{1}{r} dr = 4\pi h K_2 \alpha \ln \frac{R_2}{R_1}. \quad (3.40)$$

For the helical solutions, the energy has to be numerically calculated. Notice that the energy only depends on the ratio  $R_2/R_1$ : Fig. 2 shows the comparisons between the energies as a function of  $M = \ln(R_2/R_1)$  for different values of  $\alpha$ . We set  $k_3 = 1$  and let  $k_2$  change.

The  $\alpha$  values in Panel (a) correspond to the situation when there is only one positive solution  $\psi(R_1)$  of (3.31). When  $\alpha = 0.3$ , the concentric circle solution is preferred because it has a lower energy than the helical configuration.

When  $\alpha = 0.4$ , the helical configuration has a lower energy for a limited range of  $M$ . These two curves show that, when  $M \rightarrow \infty$ , the energy diverges faster than that of the concentric-circle configuration. This is consistent with Remark 3.2. When  $\alpha = 0.5$  and 1, the helical solution has a higher energy for smaller  $M$  and becomes preferable for large  $R_2/R_1$ . Moreover, these two curves becomes horizontal when  $M \rightarrow \infty$ , which is also consistent with the statement in Remark 3.3.

In the figures of panel (b),  $\alpha$  is set to be equal to 10. We have shown in Fig. 1 that there exist two positive solutions of  $\psi(R_1)$  for a particular range of  $a < M < \pi/4$ . One is marked as small  $\psi(R_1)$  and the other as large  $\psi(R_1)$ . In the case  $M \rightarrow a^+$ , the two helical solutions become identical. When  $M \rightarrow (\pi/4)^-$ , the small  $\psi(R_1)$  solution degenerates to the trivial concentric-circle solution, thus the small  $\psi(R_1)$  branch vanishes when  $M < a$  or  $M > \pi/4$ . The solution corresponding to large  $\psi(R_1)$  exists for  $M \geq a$ . We note that the helical configuration in this case is always preferred compared with the concentric-circle configuration. Moreover, the small  $\psi(R_1)$  branch is preferred when  $M$  is small; the large  $\psi(R_1)$  branch is preferred when  $M$  is large. However, at the (right) intersection of the two energy curves of the helical configurations, the values of  $\psi(R_1)$  are distinct. This suggests that the phase transition between these two helical configurations, as  $M$  changes through the threshold value, is not smooth.

### (d) Capsid with core energy: variable $R_1$ with fixed $R_2$

Next, we consider the total energy that consists of the sum of the ordered plus the disordered contributions, with the unknown fields being  $\psi = \psi(r)$  and the real number  $R_1 \geq 0$ :

$$\begin{aligned} E_{\text{total}}[\psi, R_1] &= E_{\text{disorder}}[R_1] + E_{\text{order}}[\psi] \\ &= 2\pi h \left[ \nu R_1^2 + 2\sigma R_1 + 2 \int_{R_1}^{R_2} \left( K_2 \left| \frac{\sin(2\psi)}{2r} - \psi_r + \tau \right|^2 + K_3 \frac{\cos^4 \psi}{r^2} \right) r dr \right]. \end{aligned} \quad (3.41)$$

Notice that  $E_{\text{order}}[\psi]$  also depends on  $R_1$ . The critical points satisfy the equations

$$\frac{\delta E_{\text{total}}}{\delta \psi} = 0 = \frac{\partial E_{\text{total}}}{\partial R_1}. \quad (3.42)$$

It follows that the governing equation for  $\psi(r)$  and the corresponding boundary conditions are again given by Eq. (3.10) and (3.11), respectively. The second equation in (3.42) gives the relation

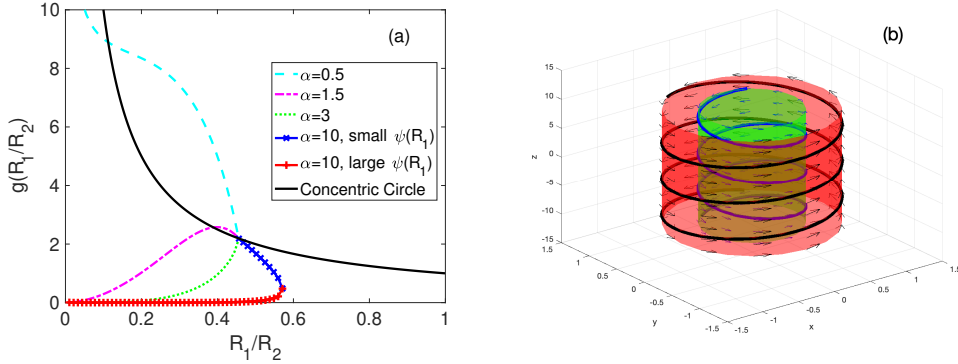


**Figure 3.** (a) Plot of the function  $g(R_1/R_2)$  of Eq. (3.44) corresponding to concentric circle vector fields (black line) and to helical vector fields. The purple curve shows that, for suitable values of  $\nu$  and  $\sigma$ , two solutions  $R_1$  exist for  $\alpha = 1.5$ , the stable one corresponding to the larger value of  $R_1$ . Note that, the plots of  $g(R_1/R_2)$  for  $\alpha = 10$ , show the two analytically studied solution branches. (b) Plot of two opposite-handed helix segments on different cylinders.

satisfied by the unknown quantity  $R_1$ ,

$$\nu R_1 + \sigma = \left[ K_2 \left| \frac{\sin(2\psi(R_1))}{2R_1} - \psi_r(R_1) + \tau \right|^2 + K_3 \frac{\cos^4 \psi(R_1)}{R_1^2} \right] R_1. \quad (3.43)$$

We will again consider the case  $\tau = 0$  and Substitute the natural boundary conditions (3.11) into (3.43) yields the equation

$$\nu R_2^2 \frac{R_1}{R_2} + \sigma R_2 = g(R_1/R_2) \triangleq K_2 \frac{\sin^2(2\psi(R_1))}{R_1/R_2} + K_3 \frac{\cos^4 \psi(R_1)}{R_1/R_2}. \quad (3.44)$$

Here we used the fact that,  $\psi(R_1)$  only depends on the ratio  $R_1/R_2$ , determined by equations (3.18) or (3.31). Thus  $R_1/R_2$  (or equivalently  $R_1$ ) and  $\psi(R_1)$  could be obtained through a set of algebraic equations, without solving the boundary value problem (3.10) and (3.11).

**Remark 3.9.** Before discussing the solvability of Eq.(3.44), we carry out a simple calculation that gives insight to the possible structure of solutions, according to the parameter values. Introducing the variable  $z = \cos^2 \psi(R_1)$ , we rewrite the former as a quadratic equation on  $z$ ,

$$\nu R_1 + \sigma = \frac{1}{R_1} \left[ N z^2 + 4K_2 z \right], \quad N := (K_3 - 4K_2) \quad (3.45)$$

Solving it provides a relationship between  $\cos^2 \psi(R_1)$  and  $R_1$ , according to the sign of  $N$ . Specifically, (a) there is a single branch relationship between  $z$  and  $R_1$ , provided  $N \geq 0$  (equivalently,  $\alpha \geq 4$ ), and (b) two possible branches otherwise (i.e.  $\alpha < 4$ ).

### (i) Determine the inner core radius $R_1$

We now discuss the numerical solution of Eq.(3.44). In Fig. 3, we represent the graphs of the function  $g(R_1/R_2)$  in Eq.(3.44), for  $\psi(R_1)$  corresponding to concentric circle vector fields as well as to helical ones, and for several choices of the parameter  $\alpha$ . These curves illustrate all possible shapes of  $g(R_1/R_2)$ . Solutions of Eq. (3.44) are then given by intersections of such curves with the line  $\nu R_2^2 (R_1/R_2) + \sigma R_2$ . We observe that, given a pair  $(\nu, \sigma)$  for which an intersection with a graph of  $g(R_1/R_2)$  with negative slope occurs, subsequent increase of  $\sigma$ , with  $\nu$  fixed, causes the value of  $R_1$  at the intersection to decrease; this is also the case, when  $\nu$  increases while keeping

$\sigma$  fixed. We also observe that, if on the left of the location of the intersection, the straight-line is above the curve of  $g$ , the energy increases with increasing  $R_1$ ; otherwise, the energy decreases with increasing  $R_1$ .

We now summarize the solvability of Eq. (3.44) as follows.

For the concentric-circle curve: (1) In the case of no intersection (corresponding to small  $\nu$  and  $\sigma$ ), then the stable configuration is  $R_1 = 1$ , with the full inner capsid region being disordered; (2) If there is one intersection, then the concentric-circle configuration is stable in  $R_1$ .

For  $\alpha = 0.5$ : (1) If there is an intersection, then the helical configuration is stable in  $R_1$ ; (2) If there is no intersection, then the stable configuration is determined by the concentric-circle curve.

For  $\alpha = 1.5$ : there might be two intersections, (1) The helical configuration with  $R_1 = 0$  is stable in  $R_1$ ; (2) If there is one intersection that the straight-line crosses the curve from above, then it is unstable; (3) If there is one intersection that the straight-line crosses the curve from below, then it is stable in  $R_1$ .

For  $\alpha = 3$ : (1) The helical configuration with  $R_1 = 0$  is stable in  $R_1$ ; (2) If there is an intersection, then the helical configuration is unstable in  $R_1$ .

For  $\alpha = 10$ , there are two branches of curves: (1) The helical configuration with  $R_1 = 0$  is stable in  $R_1$ ; (2) If there is one intersection with the lower curve, then it is unstable. The configuration where the two branches meet is stable in  $R_1$ ; (3) If there is one intersection with the upper curve, it is stable in  $R_1$ .

## (ii) Comparison with data from a set of bacteriophages

We start exploring the parameters  $K_2$ ,  $K_3$ ,  $\nu$  and  $\sigma$  of the model. Following Tzilil et al. [44], we express

$$K_3 = K_B T L_p m_0, \quad (3.46)$$

where,  $K_B$  is the Boltzmann constant,  $T$  the absolute temperature,  $m_0$  represents the linear density of DNA in the capsid and  $L_p$  the persistence length. The quantity  $m_0$  represents the linear density of DNA in the capsid and has dimensions of square inverse of the length. Table 1 lists the value of  $m_0$  for a sample of four viruses. For instance, for T4, we estimate  $m_0 = 1/(\pi(d_0/2)^2) = 0.221\text{nm}^{-2}$  ( $d_0 \approx 2.4\text{nm}$ ), and taking  $T = 300\text{K}$  gives

$$K_3 = 5 \times 10^{-11} \text{J/m}. \quad (3.47)$$

In [27], we take guidance from the theory of Onsager for lyotropic liquid crystals, to obtain expressions for the isotropic modulus  $\nu$  and the surface tension  $\sigma$ , and assume that they are functions of the (DNA) molar concentration  $c$  [45]. We adopt the expressions

$$\nu = \nu_0(c) \frac{K_B T}{R_2^3}, \quad \sigma = \sigma_0(c) \frac{K_B T}{L_p d_0}. \quad (3.48)$$

Since, to our knowledge, no molecular theory is available to determine the dimensionless parameters  $\nu_0$  and  $\sigma_0$ , and, likewise, we do not have an expression for  $K_2$  either, we proceed to estimate these three quantities from the data shown in the table. (The analogous approach followed in [27], and taking the capsid to be a sphere with the DNA arranged in concentric circles, gives  $\nu_0 = 23$  and  $\sigma_0 = 0.388$ ).

Prior to estimating  $\nu_0$  and  $\sigma_0$ , and taking into account that for DNA  $\alpha > 1$  holds, the stability properties listed in Section 3(d)(i) indicate that the solution  $R_1$  in the graphs shown in Fig. 3 lies either on the *concentric circle* branch or on the monotonically decreasing portion corresponding to  $\alpha = 10$ . Moreover, as the experimental values of  $\frac{R_1}{R_2}$  shown in Table 1 indicate, the solutions for the viruses T4, T7 and  $\epsilon 15$  are located in the latter branch, whereas that for T5 belongs to the concentric circle one. Also, for  $\alpha = 10$ , the largest possible value of  $R_1$  is where the blue and red curves meet. The results for  $\alpha = 10$  generalize to the case that  $\alpha$  is large: the graph of  $g(\cdot)$  has two branches, with the system having a stable helical configuration corresponding to the largest possible value of  $R_1$ . On the other hand, if  $0 < \alpha$  is relatively small, such that  $g(\cdot)$  has a single branch, then the stable configuration becomes  $R_1 = 1$ , with inner capsid region being disordered.

Virus	$L_p$ (nm)	$d_0$ (nm)	$c$	$L$ (nm)	$R_2$ (nm)	$R_1/R_2$	$m_0$ ( $\text{m}^{-2}$ )
T4	55.60	2.40	21.37	55047.6	40.00	0.5500	$0.22 \times 10^{18}$
T5	58.38	2.94	17.85	39423.8	42.00	0.4286	$0.147 \times 10^{18}$
T7	52.88	2.60	18.17	12932.0	26.05	0.5889	$0.18 \times 10^{18}$
$\epsilon 15$	53.90	2.55	13.98	12846.0	28.37	0.5735	$0.574 \times 10^{18}$

**Table 1.** Physical measurements of four different bacteriophages [27]. The symbol  $L_p$  denotes the persistence length of a DNA chain of length  $L$ , effective diameter  $d_0$ , molar concentration  $c$  in a sphere-like capsid of radius  $R_c$  with a measured radius  $r_c$  of the disordered core.  $m_0$  represents the linear density. T4 [2, 3]; T5 [4]; T7 [1];  $\epsilon 15$  [5].

In order to fit the curves with the experimental data of  $R_1/R_2$  shown in Table 1, we appeal to a scaling argument and estimate the value  $\nu_0 \sim 500$  so that  $\nu R_2^2/K_3 \sim 1$ . With the appropriate choice of  $\sigma_0$ , this yields intersections between the straight line and the graph of  $g(\cdot)$ , in the stable range of the helical curves and the concentric-circle curves, at values  $R_1/R_2 \approx 0.4 \sim 0.6$ .

#### 4. A filament reconstruction

In the previous sections, we have obtained a vector field  $\vec{n}$ , parametrized by the angle  $\psi$  that forms with the horizontal azimuthal vector  $\vec{e}_\theta$  (3.3), that minimizes the total energy (3.42). In this section, we construct a smooth curve, a *filament*, that starting at a given point at the entrance of the capsid, remains tangent to  $\vec{n}$  at every point. We recall the invariance property of nematic liquid crystals to the change  $\pm \vec{n}$  that allows us to replace the oriented vector field with the corresponding line field.

We consider an achiral liquid crystal, with  $\tau = 0$ , in which case, if  $\psi(r)$  is the minimizing angle  $-\psi(r)$  is also an energy minimizer, with the same energy. Moreover,  $\pm \psi$  represent the right and left handed helices, respectively. The reconstructed filament consists of piecewise helical strands over cylinders of radius  $r_i$ ,  $i = 1, \dots, N$ , with alternating handedness and connected by interpolating smooth curves.

For a given  $\epsilon > 0$ , let the point  $(r_1 = R_2 - \epsilon, \theta = 0, z = 0)$  represent the location where the DNA segment enters the capsid. The number  $\epsilon$  is taken to be of the order of the capsid thickness, that we assume to be comparable to the effective diameter of the DNA filament  $d_0$ . The reconstruction of the center axis of the DNA curve of length  $L > 0$  inside a cylindrical capsid of radius  $R_2$  and height  $2h$  starts with the observation that the sub-filament of length  $0 < L_1 \leq L$  is organized in piece-wise helices over a discrete collection of cylinders of radius  $r_i$ ,

$$R_1 + \epsilon \leq r_i \leq R_2 - \epsilon, \quad i = 1, 2, \dots, N, \\ r_1 = R_2 - \epsilon, \quad r_2 = r_1 - d(r_1), \dots, r_N = r_{N-1} - d(r_{N-1}), \quad (4.1)$$

where  $N$  a positive integer, and  $d(r)$  is the pitch of the helix on the cylinder of radius  $R_1 < r < R_2$ , both to be determined. We also take the distance between two neighbouring cylinders of radius  $r = r_i$  and  $r = r_{i+1}$  to be  $d(r_i)$ , providing the same spacing as that between neighboring segments of the helix on  $r = r_i$ . The core radius  $R_1 > 0$ , also resulting from the minimization problem, allows us to calculate  $N$ : from (4.1),  $N$  is the largest integer so that  $r_{N+1} \leq R_1$ . The length of the ordered DNA is then

$$L_1 = \sum_{i=1}^N L_1^i + O(\epsilon), \quad (4.2)$$

where  $L_1^i$  is the length of the helix on the cylinder of radius  $r_i$ . The correction term in the above sum accounts for the length of the curves connecting the helical segments. The length of the disordered DNA is then  $L_2 = L - L_1$ .

**Remark 4.1.** We assume that the full genome is being packed, and it is sufficiently long to fill the entire capsid. Modeling the packing of a short genome should include the nematic order parameter that keeps track of the local DNA concentration.

Let  $s \in (0, L_1)$  denote the arc length parameter of the DNA center curve,  $\vec{r} = \vec{r}(s)$ . We recall that the vector field representation of a helix on the cylinder of radius  $r > 0$ , is given by the vector equation

$$\vec{r}(s) = r\vec{e}_r(\theta(s)) + z(\theta(s))\vec{e}_z, \quad s \in [s_i, s_{i+1}], \quad (4.3)$$

Here  $0 < s_i < s_{i+1} < L_1$  represent the arc length values such that  $z(\theta(s_i)) = 0$  and  $z(\theta(s_{i+1})) = h$ , in the case that the curve is spooling along the positive  $z$ -direction, with the opposite signs otherwise. Furthermore, we seek  $\vec{r}(s)$  such that, at the point corresponding to the cylindrical coordinates  $(r_i, \theta(s), z(\theta(s)))$  is tangent to the vector field  $\vec{n}$ . That is, we require

$$\frac{d\vec{r}}{ds} = \vec{n}(\theta(s); r) = \cos \psi(r)\vec{e}_\theta(\theta(s)) + \sin \psi(r)\vec{e}_z, \quad (4.4)$$

$$s \in [s_i, s_{i+1}], \quad \vec{r}(s_i) = r_i\vec{e}_r. \quad (4.5)$$

Calculating

$$\frac{d\vec{r}}{ds} = \frac{d\vec{r}}{d\theta} \frac{d\theta}{ds} = (r\vec{e}_\theta + \frac{dz}{d\theta}\vec{e}_z) \frac{d\theta}{ds}, \quad (4.6)$$

and combining it with (4.5), we obtain

$$\frac{d\theta}{ds} = \frac{1}{r} \cos \psi(r), \quad \frac{dz}{d\theta} \frac{d\theta}{ds} = \sin \psi. \quad (4.7)$$

Integrating the latter on the surface of cylinder of radius  $r$ ,  $R_1 < r < R_2$ , we obtain

$$\theta(s) = \frac{s}{r} \cos \psi(r) + C_1, \quad z(s) = s \sin \psi(r) + C_1 r \tan \psi(r) + C_2, \quad (4.8)$$

where  $C_1$  and  $C_2$  are arbitrary constants.

**Remark 4.2.** In the special case of  $R_1 = 0$ , Eq. (3.23), we get

$$\theta(s) = 2 \frac{R_2}{r^2 + R_2^2} s, \quad z(s) = \frac{R_2^2 - r^2}{R_2^2 + r^2} s. \quad (4.9)$$

Note that, in calculating  $\sin \psi$  from its cosine, we have chosen the positive sign, this being consistent with the convention that curve starts at  $z = 0$  and it spirals towards the positive  $z$ -axis.

Next, with a simple calculation, we get the pitch  $d$  of the helix in (4.8). Let us consider a point of the helix on the cylinder of radius  $r$  corresponding to the arc length  $s > 0$ , and a second point on the same helix but at the location  $s + l$ ,  $l > 0$ . We let  $l > 0$  and  $d > 0$  be such that

$$\theta(s + l) = \theta(s) + 2\pi, \quad z(\theta(s + l)) = z(\theta(s)) + d(r). \quad (4.10)$$

The latter, together with equations (4.8), gives  $d(r) = l \sin \psi(r)$  and  $l = 2\pi r \sec \psi$ . Hence

$$d(r) = 2\pi r \tan \psi(r). \quad (4.11)$$

The plots in Figure 1 (a) show that  $\psi(r)$  is very small (near 0) for  $r$  close to  $R_2$ . This indicates that the outer cylindrical layers have higher filament concentration (here measured as  $\frac{h}{d(r)}$ ) than the inner ones, as consistently shown in experiments. Also, from figure 1 (a), we see that the overall values of  $\psi$  decrease as  $K_2$  increases, that is the angles are smaller for higher twist energy penalty, also to be expected.

We obtain the equation of the centerline curve on subsequent cylindrical layers, located at  $r_1, r_2, \dots, r_N$ , respectively. The independent segments in each cylinder are connected by interpolating lines,  $\mathcal{U}$ -turns, mimicking inter layered spooling curves, resulting on a globally smooth curve.

The reconstructed DNA center line is a piece-wise smooth helical curve, consisting of ordered strands as in (4.6, 4.8) connected by interpolating segments.

*First layer.* Assuming that the DNA is spooled counterclockwise from the location  $r = r_1$  near capsid inner wall to the inner core, the first segment corresponds to equations (4.8) subject to the initial conditions

$$\theta(0) = 0 \quad \text{and} \quad z(0) = -h, \quad s_0 := 0, \quad (4.12)$$

that is,

$$\theta(s) = \frac{s}{r_1} \cos \psi(r_1), \quad z(s) = \sin \psi(r_1)s - h, \quad (4.13)$$

We have seen in the previous sections that for the energy minimizing vector field  $0 \leq \psi(r) \leq \frac{\pi}{2}$  for  $r \in [R_1, R_2]$ , with  $\psi(r) \neq 0$  for  $r < R_2$ . This guarantees  $\sin \psi(r) \neq 0$ , for  $r < R_2$ . Note that the curve (4.3, 4.13) reaches the top of the capsid  $z = h$  for  $s$  such that

$$s = \frac{2h}{\sin \psi(r_1)} := s_1. \quad (4.14)$$

We observe that the quantity  $s_1$  gives the length of the helix segment, on the surface of the cylinder  $r = r_1$ , running from  $z = -h$  to  $z = h$ . Furthermore, let us denote

$$\theta_1 = \theta(s_1) \quad \text{and} \quad P_1 := (r_1, \theta_1, h). \quad (4.15)$$

*Second layer.* The second layer, the cylinder of radius  $r_2 = r_1 - d(r_1)$ , is covered by the helix (4.8) with angle  $-\psi(r_2)$ . The initial point is  $P_2 = (r_2, \theta_2, h - d(r_1))$ , with  $\theta_2$  determined according to the *connection condition* established next. So, the helical segment corresponds to the curve (4.8), with  $r = r_2$  and  $\theta \leq \theta_2$ , up to reaching  $z = 0$ .

*Connecting layer.* We construct an interpolating curve that joins the DNA segments on two consecutive cylinders, from the outer to the inner one. The smooth curve consists of two segments, but running counterclockwise, an upward one from  $(r_1, 0, h - d(r_1))$  to  $(r_1, \pi, h)$ , and a second segment starting at the point  $(r_1, \pi, h)$  running downwards towards  $(r_2, \theta_2, h - d(r_2))$ . The construction of the connecting layer segments is shown in the supplementary material.

## 5. Conclusions

We have presented a model of packaged DNA in a cylindrical capsid based on the duality of vector field and filament approach. We have shown that the model includes fundamental features some of them encountered in separate earlier models, such as the hexagonal crystal structure of DNA cross-sections. Our work also generalizes the inverse spooling assumption that has been key to earlier research and replaces it for fully helical configurations of the vector field able to sustain, both, twist and bending. By assigning an isotropic energy to the capsid core, we characterize its optimal size. Solutions of our model include the concentric circle states of earlier works. We show how from such states helical configurations bifurcate, with respect to the parameter that represents the ratio of the bending to the twist modulus. The assumption of Dirichlet boundary conditions on the capsid wall may be unreasonably restrictive and possibly misrepresent the role of the proteins there. In future work, we will relax it by assigning an anchoring energy to the capsid wall. Furthermore, in the case that such an energy is anisotropic, it may allow for corners and facets, consistent with the icosahedral geometry of the capsid. For simplicity, we do not incorporate the scalar order parameter variable of our earlier work that helps quantify the density of the DNA [24]. The work presented here is purely mechanical with no electrostatic contributions of the DNA and the environmental ions taken into account as done in our previous work [25]. The latter issues as well as the extension to capsid shapes other than cylindrical can be computationally accomplished by numerical techniques. Finally, we point out the ideal nature of the reconstructed filament in that it does not account for knots. This issue is the subject of follow up work.

**Funding.** This work was partially supported by National Science Foundation grants DMS-1817156 (J.A. and M.V.), DMS-1816740 (M.C.C. and P.L.), DMS-1729538 (D.G.), and DMS-1555222-CAREER, DMS-2111474 (S.W.).

## References

- 1 M.E Cerritelli, N. Cheng, A.H. Rosenberg, C.E. McPherson, F.P. Booy, and A. Steven. Encapsidated conformation of bacteriophage T7 DNA. *Cell*, 91(2):271–280, 1997.
- 2 N.H. Olson, M. Gingery, and T.S. Eiserling, F.A. and Baker. The structure of isometric capsids of bacteriophage T4. *Virology*, 279(2):385–391, 2001.
- 3 V.V. Mesyanzhinov. Bacteriophage T4: structure, assembly, and initiation infection studied in three dimensions. *Advances in Virus Research*, 63:287–352, 2004.
- 4 G. Effantin, P. Boulanger, E. Neumann, L. Letellier, and J.F. Conway. Bacteriophage T5 structure reveals similarities with HK97 and T4 suggesting evolutionary relationships. *Journal of Molecular Biology*, 361(5):993–1002, 2006.
- 5 W. Jiang, J. Chang, J. Jakana, P. Weigle, J. King, and W. Chiu. Structure of epsilon15 bacteriophage reveals genome organization and DNA packaging/injection apparatus. *Nature*, 439(7076):612–616, 2006.
- 6 F. Guo, Z. Liu, P. Fang, Q. Zhang, E.T. Wright, W. Wu, C. Zhang, F. Vago, Y. Ren, J. Jakana, et al. Capsid expansion mechanism of bacteriophage t7 revealed by multistate atomic models derived from cryo-em reconstructions. *Proceedings of the National Academy of Sciences*, 111(43):E4606–E4614, 2014.
- 7 A. Huet, R.L. Duda, P. Boulanger, and J.F. Conway. Capsid expansion of bacteriophage t5 revealed by high resolution cryo-electron microscopy. *Proceedings of the National Academy of Sciences*, 116(42):21037–21046, 2019.
- 8 G.P. Lomonosoff and C. Wege. Tmv particles: the journey from fundamental studies to bionanotechnology applications. *Advances in Virus Research*, 102:149–176, 2018.
- 9 A. Leforestier. Polymorphism of DNA conformation inside the bacteriophage capsid. *Journal of Biological Physics*, 39(2):201–213, 2013.
- 10 A. Leforestier and F. Livolant. The bacteriophage genome undergoes a succession of intracapsid phase transitions upon DNA ejection. *Journal of Molecular Biology*, 396(2):384–395, 2010.
- 11 J. Lepault, J. Dubochet, W. Baschong, and E. Kellenberger. Organization of double-stranded DNA in bacteriophages: a study by cryo-electron microscopy of vitrified samples. *The EMBO Journal*, 6(5):1507–1512, 1987.
- 12 F. Livolant, A.M. Levelut, J. Doucet, and J.P. Benoit. The highly concentrated liquid-crystalline phase of DNA is columnar hexagonal. *Nature*, 339(6227):724–726, 1989.
- 13 T.E. Strzelecka, M.W. Davidson, and R.L. Rill. Multiple liquid crystal phases of DNA at high concentrations. *Nature*, 331(6155):457–460, 1988.
- 14 W.C. Earnshaw, J. King, S.C. Harrison, and F.A. Eiserling. The structural organization of DNA packaged within the heads of T4 wild-type, isometric and giant bacteriophages. *Cell*, 14(3):559–568, 1978.
- 15 P.K. Purohit, J. Kondev, and R. Phillips. Mechanics of DNA packaging in viruses. *Proceedings of the National Academy of Sciences*, 100(6):3173–3178, 2003.
- 16 N.V. Hud. Double-stranded DNA organization in bacteriophage heads: an alternative toroid-based model. *Biophysical Journal*, 69(4):1355–1362, 1995.
- 17 W.C. Earnshaw and S.C. Harrison. DNA arrangement in isometric phage heads. *Nature*, 268 (5621):598–602, 1977.
- 18 P.K. Purohit, J. Kondev, and R. Phillips. Force steps during viral DNA packaging? *Journal of the Mechanics and Physics of Solids*, 51(11-12):2239–2257, 2003.
- 19 J. Kindt, S. Tzilil, A.B.-Shaul, and W.M. Gelbart. DNA packaging and ejection forces in bacteriophage. *Proceedings of the National Academy of Sciences*, 98(24):13671–13674, 2001.
- 20 J. Arsuaga, R. Tan, M. Vazquez, and S.S. Harvey. Investigation of viral DNA packaging using molecular mechanics models. *Biophysical Chemistry*, 101:475–484, 2002.

21 S.R. Casjens. The DNA packaging nanomotor of tailed bacteriophages. *Nature Reviews Microbiology*, 9(9):647–657, 2011.

22 A.S. Petrov, M.B. Boz, and S.C. Harvey. The conformation of double-stranded DNA inside bacteriophages depends on capsid size and shape. *Journal of Structural Biology*, 160:241–248, 2007.

23 A.S. Petrov, K. Lim-Hing, and S.C. Harvey. Packaging of DNA by bacteriophage epsilon15: structure, forces, and thermodynamics. *Structure*, 15(7):807–812, 2007.

24 S. Walker, J. Arsuaga, L. Hiltner, M.C. Calderer, and M. Vazquez. Fine structure of viral dsDNA encapsidation. *Physical Review E*, 101(2):022703, 2020.

25 P. Liu, J. Arsuaga, M.C. Calderer, D. Golovaty, M. Vazquez, and S. Walker. Ion-dependent DNA configuration in bacteriophage capsids. *Biophysical Journal*, 2021.

26 W.S. Klug and M. Ortiz. A director-field model of DNA packaging in viral capsids. *Journal of the Mechanics and Physics of Solids*, 51(10):1815–1847, 2003.

27 L. Hiltner, M.C. Calderer, J. Arsuaga, and M. Vázquez. Chromonic liquid crystals and packing configurations of bacteriophage viruses. *Philosophical Transactions of the Royal Society A*, 379 (2201):20200111, 2021.

28 F. Hang, F. Lin, and Y. Yang. Existence of Faddeev knots. *Surveys in Differential Geometry*, 13 (1):149–222, 2008.

29 H. Shin and G.M. Grason. Filling the void in confined polymer nematics: Phase transitions in a minimal model of dsDNA packing. *Europhysics Letters*, 96(3):36007, 2011.

30 L. Lucchetti, T.P. Fraccia, G. Nava, T. Turiv, F. Ciciulla, L. Bethge, S. Klussmann, O.D. Lavrentovich, and T. Bellini. Elasticity and viscosity of dna liquid crystals. *ACS Macro Letters*, 9(7):1034–1039, 2020.

31 F. Bethuel, H. Brezis, B.D. Coleman, and F. Hélein. Bifurcation analysis of minimizing harmonic maps describing the equilibrium of nematic phases between cylinders. *Archive for Rational Mechanics and Analysis*, 118(2):149–168, 1992.

32 D. Golovaty, Y. Kim, O.D. Lavrentovich, M. Novack, and P. Sternberg. Phase transitions in nematics: textures with tactoids and disclinations. *Mathematical Modelling of Natural Phenomena*, 15:8, 2020.

33 S. Relaix and M. Mitov. Polymer-stabilised cholesteric liquid crystals with a double helical handedness: influence of an ultraviolet light absorber on the characteristics of the circularly polarised reflection band. *Liquid Crystals*, 35(8):1037–1042, 2008.

34 F. Gaill and Y. Bouligand. Alternating positive and negative twist of polymers in an invertebrate integument. *Molecular Crystals and Liquid Crystals*, 153(1):31–41, 1987.

35 N. Katsonis, E. Lacaze, and A. Ferrarini. Controlling chirality with helix inversion in cholesteric liquid crystals. *Journal of Materials Chemistry*, 22(15):7088–7097, 2012.

36 R. Zandi, B. Dragnea, A. Travesset, and R. Podgornik. On virus growth and form. *Physics Reports*, 847:1–102, 2020.

37 D. Svenšek and R. Podgornik. Confined chiral polymer nematics: Ordering and spontaneous condensation. *Europhysics Letters*, 100(6):66005, 2013.

38 D. Svenšek, G. Veble, and R. Podgornik. Confined nematic polymers: Order and packing in a nematic drop. *Physical Review E*, 82(1):011708, 2010.

39 T. Curk, J. Farrell, J. Dobnikar, and R. Podgornik. Spontaneous domain formation in spherically confined elastic filaments. *Physical Review Letters*, 123(4):047801, 2019.

40 R. Hardt, D. Kinderlehrer, and F.H. Lin. Existence and partial regularity of static liquid crystal configurations. *Communications in Mathematical Physics*, 105(4):547–570, 1986.

41 J.K. Hale. *Ordinary differential equations*. Krieger, New York, 1980.

42 L.W. Black, W.W. Newcomb, J.W. Boring, and J.C. Brown. Ion etching bacteriophage t4: support for a spiral-fold model of packaged dna. *Proceedings of the National Academy of Sciences*, 82(23):7960–7964, 1985.

43 C. Williams, P. Pierański, and P.E. Cladis. Nonsingular  $s=+1$  screw disclination lines in nematics. *Physical Review Letters*, 29(2):90, 1972.

44 S. Tzlil, J.T. Kindt, W.M. Gelbart, and A. Ben-Shaul. Forces and pressures in DNA packaging and release from viral capsids. *Biophysical Journal*, 84(3):1616–1627, 2003.

45 L. Onsager. The effects of shape on the interaction of colloidal particles. *Annals of the New York Academy of Sciences*, 51(4):627–659, 1949.